

Doping in garnet-type electrolytes: kinetic and thermodynamic effects from molecular dynamics simulations

Matthieu Mottet, Aris Marcolongo, Teodoro Laino, and Ivano Tavernelli*

IBM Research GmbH, Zurich Research Laboratory, 8803 Ruschlikon

(Dated: January 25, 2019)

Abstract

To shed light on the impact of doping on the conductivity of garnet-type electrolytes, we use molecular dynamics with an *ab-initio* designed force-field to investigate the complex interplay between the carrier concentration and the kinetic and thermodynamic changes induced by the addition of hypervalent dopants. We particularly focus on the effect of the distribution of the doping agents and find that there is a need to perform a proper average over the frozen disorder introduced by the doping. We observe the competing effect between the decrease in concentration of the conducting ions (Li^+) and the perturbation of the energy landscape induced by the insertion of hypervalent dopants. These two phenomena give rise to an intricate balance between thermodynamic and kinetic properties, which make the interpretation of the experiments very challenging. In particular, while the increase in the dopant concentration stabilizes the conductive cubic phase of these garnet-types materials, the kinetic effects have two distinct components acting in opposite directions. The nature of these processes is explained by means of atomistic simulations.

* ita@zurich.ibm.com

I. INTRODUCTION

The next generations of lithium batteries still face many challenges in terms of safety and stability. The key to solving many of these issues might lie in the selection of more efficient electrolytes. Until now, liquid electrolytes based on organic solvents such as ethylene carbonate or propylene carbonate have been commonly used. The general flammability of organic solvents, the risk of environmental contamination upon improper disposal of liquids [1] and the difficulties of using a liquid phase in production are some of the issues faced by these electrolytes. They have also hindered the development of future battery technologies such as Li/O₂ and Li/S. The lack of electrochemical stability of organic electrolytes in Li/O₂ batteries has been shown both experimentally [2–5] and theoretically [6, 7] to result in a loss of efficiency. Similarly, the solubility of some LiS_n compounds in the organic solvents used leads to a similar loss of efficiency over time in Li/S batteries [8]. All these issues have stimulated research efforts to find suitable electrolyte replacements. Early advances in research on solid-state electrolytes (SSE) [9, 10] have led to a high interest in these compounds. Although many candidates have been found that combine thermodynamical, chemical and electrochemical stability with reasonably high Li-ion conductivity in several chemical families, the optimal solid-state electrolyte is yet to be discovered.

Several inorganic compounds have been investigated as potential solid-state electrolytes [9, 11–13]. Candidates range from oxides to non-oxides, and crystalline to amorphous. In 2003, Thangadurai *et al.* [14] identified a new class of Li-ion conductors, the garnet-like lithium oxides. Although the first of those identified structures had relatively low conductivity ($\approx 10^{-6}$ S cm⁻¹), the high versatility of the structure allowed great improvement through composition change and doping. Among the most promising candidates, lanthanum and zirconium containing lithium oxides (LLZO) have proven to be the most promising ones, with conductivity going up to 10^{-3} S cm⁻¹ [15–17].

LLZO can be found in two phases, a tetragonal, low-conducting one, and a cubic, highly conductive one. The difference of conductivity between the two phases reaches up to 3 orders of magnitude and is mostly due to the difference in the Li network of each phase. The tetragonal structure is composed of a saturated network of 56 Li sites (8 tetrahedral, 8a, and 48 distorted octahedral, 16f and 32g). This arrangement forces the diffusion process to follow an energetically improbable, concerted mechanism. On the other hand, in the cubic

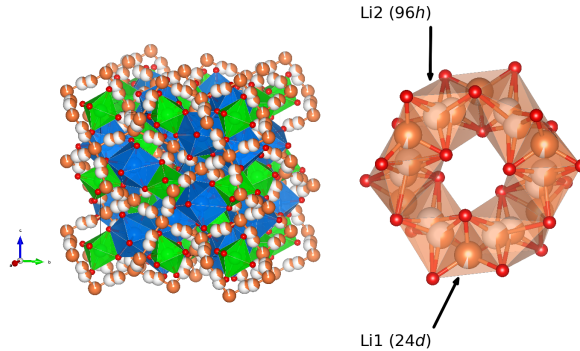


Figure 1. **Left** Structure of the cubic phase of the lithium containing garnet (LLZO). The Zr and La polyhedra are represented in green and blue respectively. **Right** Ring structure formed by the tetrahedral $24d$ and the two octahedral $96h$ Li-sites in the crystal.

phase, the distorted octahedral sites split into two energy equivalent sites ($96h$), leaving space for a hopping-type mechanism. Though the tetragonal structure is more stable at room temperature, the cubic, better conducting, phase can easily be stabilized using doping. The understanding of the mechanism of phase stabilization as a function of the conditions (doping concentration and temperature) is therefore central to guide the design of better performing solid-state electrolytes.

Computational investigations targeted at solid-states electrolytes aim at creating a deeper understanding of the various phenomena that control and influence the conductivity of a given ionic species. Although this type of investigation is often presented as the promise of the identification of better materials, most new electrolytes are still discovered by intuition or serendipity. This is because, presently, the theoretical methods available for the accurate characterization of the medium-to-long timescale needed to describe the transport process are not suited to use on large datasets. However, molecular dynamics simulations can still offer very valuable information. In particular, it can help compare the physical and chemical properties of systems differing by a set of well-controlled parameters, ranging from the atomic composition to the thermodynamic properties like temperature and pressure.

In this work we focus on a comparative study of the conductivity of doped garnets of the LLZO family. Several studies, both experimental and theoretical, have already investigated some of the effects of doping on LLZO. Three types of doping can be identified: (*i*) the substitution of Li ions by hypervalent cations such as Al [18, 19] or Ga [20], (*ii*) the substitution of the metal centers by cations such as Ce [21], Ta [22, 23], W [24, 25] and Nb [15], and (*iii*) a co-doping by more than one of the two first options [26–29].

Adams *et al.* [30], and Jalem *et al.* [20] first introduced the use of force-fields for the modelling of, respectively, Ga and Ta or Nb doped garnets. Although these force-fields could predict a cubic phase for the low temperature structure of the doped systems, neither force-field could successfully describe the cubic to tetragonal transition of the undoped structure. Klenk *et al.* [31] later showed that the stability of the undoped garnet system can be accurately described using a polarizable force-field, based on an *ad-hoc* determination of the polarizable force-field parameters. Despite the interesting results, the authors did not address the effects of doping on the structure of LLZO or its conductivity. More recently, Chen *et al.* [23], using a non polarizable force-fields, successfully described the phase transition of the undoped structure and the stabilization of the cubic phase via Ta doping. Their work focused on the understanding of the phase stabilization through changes in the occupancy of the lithium sites. However, their study did not extend to the investigation of the lithium ions dynamics.

The motivations for this work are twofold. Our long-term goal is to provide a general framework for the unsupervised parametrization of core-shell models to be used for the simulation and screening of solid-state electrolytes properties. With this work, we aim to understand the issues related to the use of this type of modelling in the description of the LLZO systems, and in particular of doped ones. We investigate in details the physics of W-doped systems, with formula $\text{Li}_{7-2x}\text{La}_3\text{Zr}_{2-x}\text{W}_x\text{O}_{12}$, from both a kinetic (barriers and conductivity) and thermodynamic (phase stability) standpoints. Our system choice was motivated by the experimental results provided by Li *et al.* [25], where several dopant concentrations and temperatures were explored using a consistent synthetic approach. Our work mainly differs from previous analysis by its focus. Our target is to resolve the effects on the dynamics resulting from the change in charge carrier concentration and from the introduction of the doping agents. To this end, we compare two doping models (*i*) an implicit model using a uniform background charge and (*ii*) an explicit model using substitution of hypervalent ions. In the second model, we introduced an additional average over the positions of the W ions to account for the frozen noise of the dopant distribution and analyze the results within the framework of spin glass theory. We show that while doping can affect the conductivity both through a depletion of the charge carriers and a potential increase of the hopping barriers by the hypervalent dopants, it also influences the thermodynamic stability of the conductive cubic phase. The delicate interplay between these two effects is

what makes the physics of doped SSE very challenging for both experimental and theoretical studies.

II. COMPUTATIONAL METHODS

In this section, we report a short description of the force-field used in this work for the characterization of the structural stability and for the analysis of the transport properties of undoped and W-doped LLZO derivatives. Classical molecular dynamics was performed using long range Coulomb interactions, short range Buckingham potentials of the form

$$U(R_{ij}) = Ae^{-\frac{R_{ij}}{\rho}} - \frac{C}{R_{ij}^6} \quad (1)$$

for all oxygen- and metal-oxygen pairs (i, j) within a cutoff distance $R_{ij} = 10\text{\AA}$, and a Dick–Overhauser core–shell model [32] to describe the polarization of the O atoms, as implemented in the LAMMPS [33] code for molecular dynamics simulations. The parameters for the polarization of the oxygen, *i.e.* the core-shell charge splitting, Y , and spring constant, k are fitted to the atomic polarization computed in the crystal environment at density functional theory (DFT) level of theory. The Buckingham parameters for the metal-oxygen pairs, Li–O, La–O and Zr–O, refined from the one used by Klenk *et al.* [31], and the value of the unit charge q were optimized using a fitting procedure based on first-principle data evaluated using DFT. All DFT calculations were carried out using the plane wave CPMD software package [34, 35]. The PBE functional and norm-conserving Goedecker pseudopotentials [36] were used in conjunction with a cutoff of 150 Ry. Only the repulsive part of the metal-oxygen pairs is considered with all other C parameters being set to 0. The optimization was carried by minimizing the sum of the mean-square errors on the forces and total energy, as well as the sum of the angular deviation of the forces, by means of the cost

function

$$\begin{aligned}
C(\{b_{\text{LiO}}\}, \{b_{\text{LaO}}\}, \{b_{\text{ZrO}}\}) = & \\
& \frac{1}{N_s} \sum_s \left(\alpha_s (E_{\text{DFT},s,i} - E_{\text{pFF},s,i})^2 \right. \\
& + \beta_s \sum_i \left| \vec{F}_{\text{DFT},s,i} - \vec{F}_{\text{pFF},s,i} \right|^2 \\
& \left. + \gamma_s \sum_i \frac{\vec{F}_{\text{DFT},s,i} \cdot \vec{F}_{\text{pFF},s,i}}{\left| \vec{F}_{\text{DFT},s,i} \right| \cdot \left| \vec{F}_{\text{pFF},s,i} \right|} \right) \quad (2)
\end{aligned}$$

where $\{b_{\text{XO}}\} = \{A_{\text{XO}}, \rho_{\text{XO}}\}$ is the parameter set that defines the Buckingham potential of the pair X–O with X={Li, La, Zr} s runs over the used structures and i over the atoms of the structure s . α , β and γ are weights used to balance the fitting procedure. The parameters for the W–O pair were obtained using the same methodology. The parameters used for this work are listed in Table I.

Pair	A (eV)	ρ (Å)	C (eVÅ ⁶)	Charge and shell
Li–O	461.30	0.3074	-	q (e) = 0.962
La–O	4420.23	0.2980	-	
Zr–O	1269.33	0.3499	-	
W–O	1397.76	0.3549	-	Y (e) = -2.75
O–O	22764.30	0.1490	27.63	k (eVÅ ⁻²) = 30.2

Table I. Force-field parameters used in this work.

All MD simulations were carried out in the isothermal- isobaric (NPT) and canonical (NVT) ensembles, with an integration timestep of 0.25 fs, using a $2 \times 2 \times 2$ supercell. A colored noise or generalized Langevin equation (GLE) thermostat for core-shell models [37, 38] was used to control the temperature of the system. The choice of the thermostat was motivated by non-negligible drifts observed in the energy when using the Nosé-Hoover thermostat with hypervalent ions present in the structure. The colored noise thermostat maximizes the adiabatic separation of the dynamics of the lightweight shells from the one of the ions while minimizing the impact on the shell dynamics. To account for a small energy transfer to the shells and maintain a stable dynamics over long simulation times, a zero temperature memory-less friction thermostat is coupled to the shells [37]. We show in Appendix B that the present use of the colored-noise thermostat has a minimal impact on the dynamical quan-

tities of interest. In the case of the NPT simulations, a Berendsen barostat was used for the pressure control with a damping parameter of 25 ps. The phase diagrams (Fig. 4) were computed using temperature increments of 120 K from 200 to 1400 K, in both directions. In the temperature range where a phase transition took place, a finer sampling performed using temperature increments of 25 K. At each temperature step, the system was equilibrated for 250 ps and statistics were collected over the subsequent 750 ps of dynamics. For the computation of the conductivity, the temperature was increased to the target temperature over 250 ps. After 250 more ps of equilibration, the positions were recorded every 0.1 ps for a duration of 4 ns. Block-averaging analysis was used to estimate the error for all the quantities computed along the trajectories. This technique relies on the division of the trajectory into long enough blocks. Each block provides an independent estimate of the quantity of interest (e.g. lattice parameter, diffusion coefficient), and the final error is derived from the standard error of the mean, reflecting the spread of the quantity measured through the different blocks [39].

Doping is used to vary the concentration of charge carriers in the structure. Each substitution introduces extra electrons/holes whose charges have to be compensated by the addition/removal of the corresponding number of Li-ions. We investigate here the substitution of Zr^{4+} ions by W^{6+} ones. To shed light on the origin of the observed changes in material properties and identify if they are triggered by the presence of hypervalent cations or by the change in carrier concentration, we compare two models: an *implicit* and an *explicit* doping protocol. In the *implicit* model the concentration of the charge carrier is changed without substituting hypervalent cations. The extra charge is compensated by a positive background charge which does not influence the forces during the dynamics. The *explicit* model incorporates the substitutions explicitly. Note that only the latter model is able to capture, in an approximate way, the local changes of the electronic structure due to the presence of the dopant. Comparison between the results of the two models can shed light on the different static and dynamical aspects at play in the doping of the garnet electrolytes.

The addition of a small fraction of dopants rises the issue of their distribution in the unit cell considered. This is particularly important since the position of the dopants remains frozen over the time of our simulations. This situation is reminiscent of the fixed disorder distribution in spin-glasses [40]. To account for the disorder of the dopant distribution, we introduce, in addition to the time average, an additional average of all measured properties

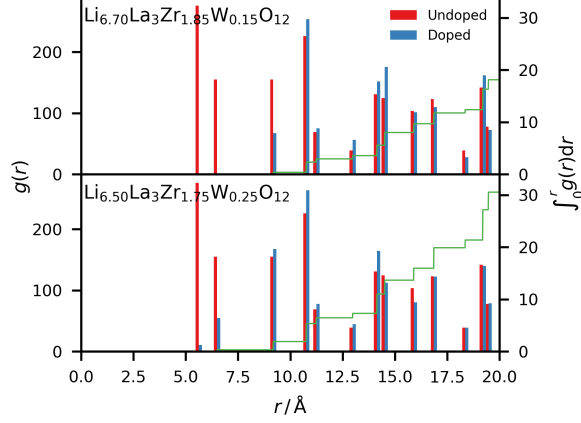


Figure 2. Radial distributions of the Zr-Zr (red) and W-W (blue) pairs respectively in the undoped and Boltzmann-distributed doped structures with doping fraction $x = 0.15$ (top) and 0.25 (bottom). The shortest distance pairs are absent at low doping concentration structure due to the increased Coulomb repulsion between the hypervalent cations. Increasing the concentration saturates the structure enough that the shortest distances are forced to be occupied but longer distances remain favoured compared to the original *bcc* Zr structure. The green curve represents the integral of the W-W radial distribution function.

over a set of structures with different dopant distributions. The expectation value of an observable J therefore becomes

$$[\langle J \rangle]_{\text{av}} = \sum_{\Gamma_D} \left(\sum_R \frac{e^{-\beta E_{\Gamma_D}(R)}}{Z_{\Gamma_D}} J_{\Gamma_D}(R) \right) \cdot P_{\Gamma_D}, \quad (3)$$

where R is the collective array of the nuclear coordinates, and Z_{Γ_D} is the partition function for a given realization of the disorder Γ_D , distributed with the probability P_{Γ_D} . In the ergodic limit and using the fact that the Γ_D degrees of freedom are frozen

$$[\langle J \rangle]_{\text{av}} = \sum_{\Gamma_D} \left(\lim_{t \rightarrow \infty} \frac{1}{t} \int_0^t J_{\Gamma_D}(R(t')) dt' \right) \cdot P_{\Gamma_D}. \quad (4)$$

The Boltzmann probability P_{Γ_D} is evaluated using a Monte-Carlo simulation in the ionic space composition [41], according to which Zr and W atoms are swapped at an effective temperature of 1200 K to mimic the dopant distribution at the usual sintering temperatures. Fig 2 shows the W-W radial distributions obtained for the Boltzmann distributed ionic configuration evaluated at two different doping concentrations, $x = 0.15$ and 0.25 . It is important to note that the W-W pair distribution obtained from a random replacement

of the Zr ions with the W atoms would overlap with the original Zr–Zr undoped pair distribution. However, one can observe a depletion of the shortest distance pairs as a result of the increased Coulomb repulsion between the hypervalent W^{6+} ions. When considering explicit doping, all reported calculations are obtained averaging over an ensemble of Boltzmann-weighted structures unless otherwise stated.

III. RESULTS

Structure analysis

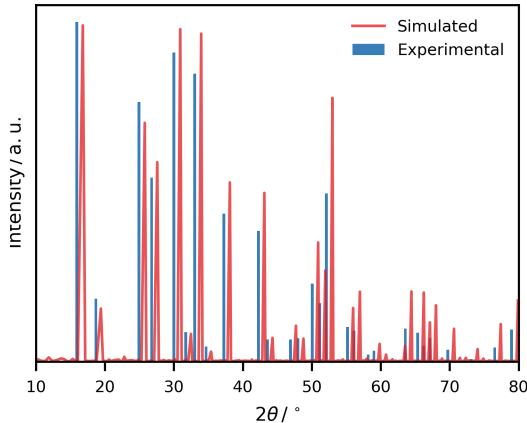


Figure 3. XRD pattern of the $Li_{6.7}La_3Zr_{1.85}W_{0.15}O_{12}$ computed from the 300 K trajectories averaged over the dopant distribution. The pattern replicates the use of Cu $K\alpha$ radiation with 2θ in the range of $10 - 80^\circ$. For comparison we display the position and amplitude of the peaks reported by Li *et al.* [25] for the same structure.

In order to assess the quality of our polarizable force-field Hamiltonian and the effects introduced by the use of the GLE thermostat, we first compare our results to experimental measurements, namely X-Ray diffraction (XRD) and lattice parameters measurements. In Fig. 3, we present the XRD pattern computed for doped structures ($x = 0.15$) from NVT trajectories and we compared it to the corresponding experimental values reported by Li *et al.* [25]. We observe that the position and amplitude of the peaks are well reproduced, even though a systematic shift is present. This is likely due to differences in the lattice parameters and effective charges on the atoms. Despite these discrepancies, these first results confirm the quality of our model and ensure a good level of trust in the interpretation of the following simulations.

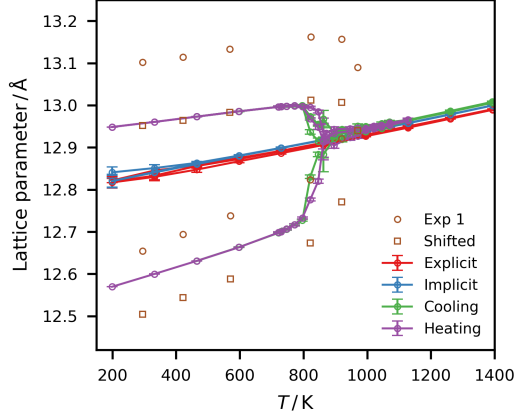


Figure 4. Lattice parameters as a function of the temperature for an undoped structure (**green** and **purple**) and doped (**blue** implicit and **red** explicit) with a doping fraction $x = 0.15$. The **brown circles** are experimental values reported by Larraz *et al.* [42]. The **brown squares** are the same experimental values shifted as to align the cubic lattice parameters. The phase transition can be observed between 800 and 900 K for the undoped structure with a small hysteresis. Both doped models successfully stabilize the cubic structure at low temperature.

Fig. 4 shows the lattice parameters obtained from our NPT simulations. In the case of the undoped system we present two different curves, the first obtained from a heating process from 200 K upwards and the second from a cooling one from 1400 K downwards. The transition from the cubic to the tetragonal phase can clearly be observed between 800 and 900 K and is characterized by a small hysteresis. The difference between the two transition temperatures is however smaller than the temperature step used. Most importantly, in the case of the doped structures, both our implicit and explicit doping models at $x = 0.15$ are able to describe the stabilization of the cubic structure at low temperature. This suggests that the stabilization of the cubic phase induced by doping is a result of the change in the lithium concentration rather than of electrostatic effects induced by the presence of the dopant itself. This is in agreement with previous studies on the subject [23]. Our model predicts quantitatively the experimental split between the lattice parameters despite a systematic shift towards smaller values. The discrepancy between our simulation and experimental measurement (as well as previously reported simulations [31, 43]) may be associated with the different force-field parametrization and with the use of the colored noise thermostat in our simulations. The difference in the equation of state of the cubic phase presented in App. A can in particular help explain the underestimation of the lattice parameter by our simulations.

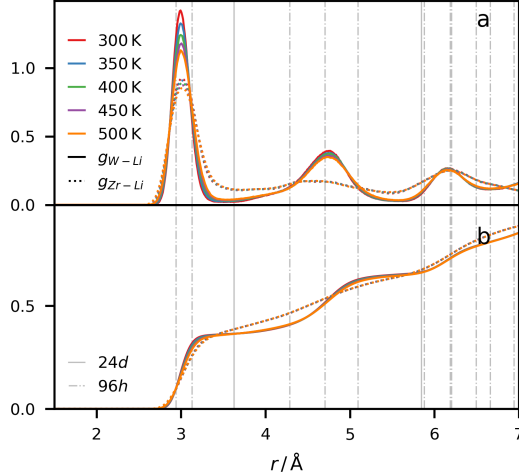


Figure 5. **a**) Radial distribution function of the Li-M pairs, M = W (**solid**) and Zr (**dotted**) for $x = 0.150$ at temperatures between 300 and 500 K. The vertical lines indicate the distances to the neighboring octahedral, 96h, (**dash-dotted**) and tetrahedral, 24d, (**solid**) crystallographic sites. **b**) Integral of the radial distribution functions presented in *a*.

Fig. 5 shows the radial distribution functions for the Zr-Li and W-Li pairs at various temperatures and their integrals for a doping of $x = 0.15$. The first coordination shell is well defined and located at the distance corresponding to the nearest two octahedral sites, respectively 2.94 and 3.13\AA . Around the Zr centers, no further coordination shell is well resolved indicating a liquid like behaviour of the ions. On the contrary, in the neighborhood of the W centers, the lithium density located beyond the first shell is pushed back by the higher coulombic repulsion and forms a second shell near the next-nearest octahedral sites at a distance of 4.7\AA . Fig. 6 shows the lithium ions distribution around a Zr and W center sampled during 8 ns of simulation. The changes described in Fig. 5 are reflected here in the depletion of the lithium density at the tetrahedral sites, cutting the lithium density into six blobs centered around the octahedral sites.

Dynamics and diffusion analysis

Dynamical properties can be directly assessed by means of molecular dynamics simulations. Velocity autocorrelation functions are valuable sources of insight for characterization of the dynamics of a system. We consider the single-particle velocity autocorrelation of the lithium ions, defined as $C_v^{\text{Li}}(t) = \left[\langle \mathbf{v}_i(t_0 + t) \mathbf{v}_i(t_0) \rangle_{i,t_0} \right]_{\text{av}}$, where $\mathbf{v}_i(t)$ is the velocity of a tagged lithium i at time t . Brackets $\langle \cdot \rangle_X$ are used to represent the averaging over the

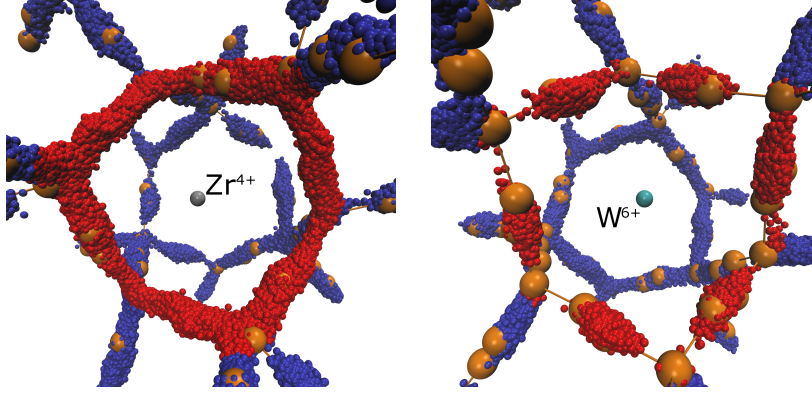


Figure 6. Representation of the lithium distribution sampled during 8 ns of simulations around a central Zr (**left**) and W (**right**) ion. The lithiums are displayed in red when within a 3.75 \AA distance from the central atom and blue otherwise. The sites of the crystallographic structures are overlaid in orange. The figure illustrates the depletion in lithium density around the tetrahedral sites in agreement with what is observed in Fig. 5 ($r = 3.6 \text{ \AA}$).

variable X . Note that by ergodicity the average over the initial time, t_0 , is equivalent to an ensemble average over initial configurations. Although the autocorrelation function displays a very fast decay, order of a few picoseconds, typical of liquid systems [44] and other fast ionic conductors [45], the diffusive process is reflected in the long time tails (see App. C). We find that the velocity autocorrelation functions in the garnet material follow a power law decay of the form τ^{-a} . For our simulations, we obtain a value of $a = 2$ in the case of the undoped cubic structure and explicitly doped material, and $a = 3$ for the implicitly doped structure. This difference in the kinetics between the explicit and implicit model can be explained by the introduction of the hypervalent W^{6+} cations in the explicit models introducing new obstacles constraining the motion of the charge carriers, since the decrease of the carrier concentration is identical. These observations are in line with the effect of the W centers on the lithium distribution in Fig. 5 and 6. The Fourier transform of $C_v^{Li}(t)$, *i.e.* the Li power spectrum, $C^{Li}(\omega)$, shows two very broad peaks at frequencies of 130 and 270 cm^{-1} for the explicitly doped system. The peaks can be connected to the presence of the two nonequivalent lithium sites in the structure (see Fig. 1).

Central to the analysis of the dynamical effects of doping is the calculation and comparison of the diffusion coefficients. To this end we compare the behaviors of the charge, D_σ , and tracer, D_{Tr} , diffusion coefficients. Both quantities can be estimated by the derivative of the long time limit of the mean-squared displacements of, respectively, the center of mass of the

particles and the particles,

$$D_{\sigma} = \left[\lim_{t \rightarrow \infty} \frac{N_{\text{Li}}}{6} \frac{\partial}{\partial t} \left\langle |\langle \mathbf{x}_i(t_0 + t) \rangle_i - \langle \mathbf{x}_i(t_0) \rangle_i|^2 \right\rangle_{t_0} \right]_{\text{av}} \quad (5)$$

$$D_{\text{Tr}} = \left[\lim_{t \rightarrow \infty} \frac{1}{6} \frac{\partial}{\partial t} \left\langle |\mathbf{x}_i(t_0 + t) - \mathbf{x}_i(t_0)|^2 \right\rangle_{i, t_0} \right]_{\text{av}} \quad (6)$$

with N_{Li} the number of Li ions in the simulation cell and $\mathbf{x}_i(t)$ the position of the Li ion i at time t . In particular, D_{σ} is directly proportional to the ionic conductivity [45]. The polynomial decay of the velocity autocorrelation function leads to a slow-down of the convergence of both the charge and particles mean square displacements used in the evaluation of the transport coefficients. The derivative of the mean square displacement can successfully be fitted to a $D_{\infty} + ct^{-(a-1)}$ function that we use to evaluate the asymptotic values of the diffusion coefficients (see details in appendix C).

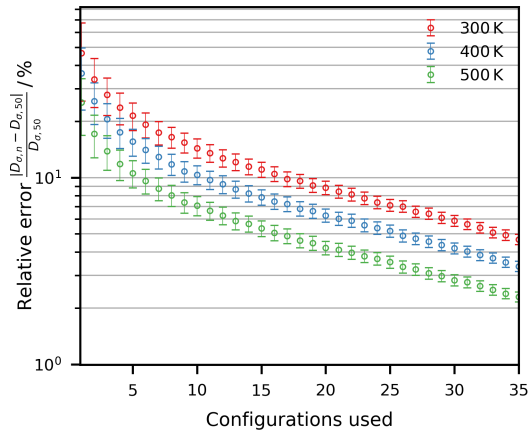


Figure 7. Relative error of $D_{\sigma,n}$, the estimator of the charge diffusion coefficient using a subset of n structures of formula $\text{Li}_{6.5}\text{La}_3\text{Zr}_{1.75}\text{W}_{0.25}\text{O}_{12}$, with respect to $D_{\sigma,50}$, used as an estimate of $D_{\sigma,\infty}$ at 300, 400 and 500 K.

When performing explicit doping, we observe large variations of the measured diffusion coefficients as a function of the dopant distribution. This effect is particularly strong at low temperatures. The convergence of the diffusion coefficient as a function of the dopant distribution is evaluated in the following way. Starting from an ensemble of 50 Boltzmann distributed dopant configurations, we computed 50 independent trajectories and corresponding charge diffusion coefficients, $D_{\sigma,i}$ with $i = 1, \dots, 50$ (using Eq. 5). The average over these values is taken as the reference diffusion coefficient $D_{\sigma,\infty} = \langle D_{\sigma,i} \rangle_i$. To estimate the convergence as a function of the number of dopant configurations k , we computed averages of

the diffusion coefficients within N_k subsets of trajectories: $D_{\sigma,I}^{(2)}$ to $D_{\sigma,I}^{(49)}$, where $D_{\sigma,I}^{(k)}$ (with $I = 1, \dots, N_k$), is an average diffusion coefficient computed using k trajectories sampled from the initial pool of 50 trajectories. Since the number of possible combinations grows as $\binom{50}{k} = \frac{50!}{k!(50-k)!}$, we apply a cutoff to N_k ($N_k \leq 10000$). The relative error for the estimated diffusion coefficients (as compared to $D_{\sigma,\infty}$) is then defined as $Z_I^{(k)} = |D_{\sigma,I}^{(k)} - D_{\sigma,\infty}|/D_{\sigma,\infty}$. The corresponding mean values, $Z^{(k)} = \langle Z_I^{(k)} \rangle_I$, and standard deviations of $Z_I^{(k)}$ as a function of k are reported in Fig. 7. An analysis of the dependence on the total simulation time is given in Appendix D. These results clearly show that, from a computational perspective, the average over different dopant configurations is indeed required in order to obtain fully converged results (see Eq. 4) that can be compared with experiments. In fact, experiments deal with measurements over a large distribution of possible dopant arrangements while simulations are limited to a single periodically replicated distribution at a time and must therefore be averaged over all relevant (Boltzmann distributed) dopant distributions.

Diffusion coefficients

The diffusion coefficients obtained after averaging over the dopant distributions at 300, 350, 400, 450 and 500 K are summarized in Fig. 8. At all temperatures our results are compatible with a linear Arrhenius behavior. For comparison, we also show the values obtained for the undoped material constrained in the cubic geometry as a reference (green lines). We first focus on the tracer diffusion coefficients, D_{Tr} , (solid lines in Fig. 8), for which we extracted an activation energy of about 0.16 eV. However, since this structure is unstable at room temperature, we can only compare our numerical results with values extrapolated from higher temperature (900 – 1400 K) measurements. Our simulations are in good agreement with the corresponding experimental activation energy estimated to be about 0.18 eV [46]. In the implicit scheme the values of the activation energies decrease compared to the undoped case to 0.13 ($x = 0.15$) and 0.08 eV ($x = 0.25$). The decrease in the number of charge carriers also correlates to an increase in the overall conductivity. This is most likely due to the increased number of empty sites allowing greater mobility of the ions. When considering the explicit model, the activation energies increase to 0.20 and 0.25 eV respectively, with an overall decrease in conductivity. This is coherent with the picture emerging from Fig. 5 and 6 where the hypervalent W ions displace some of the

Li density around them creating obstacles to the diffusion. Compared to the experimental values of 0.44 and 0.42 eV reported by Li *et al.* [25], although we underestimate the activation energy, the model correctly yields a qualitative increase in the activation energy to values similar to those expected for Ta doping [47]. Similar observations can be made for the charge diffusion coefficients (dashed line in Fig. 8).

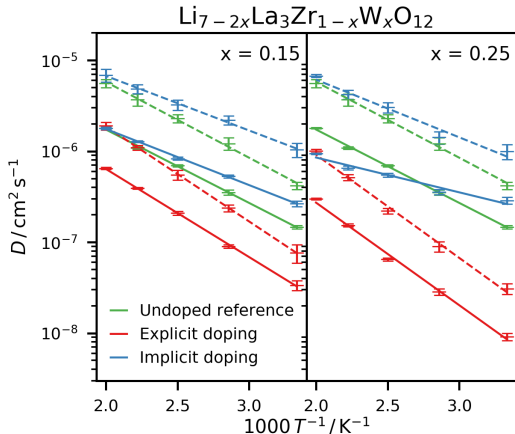


Figure 8. Tracer (**solid**) and charge (**dashed**) diffusion coefficients for doping concentrations $x = 0.15$ (**left**) and $x = 0.25$ (**right**). Simulations considering explicit and implicit doping are reported and compared with the ones obtained for a cubic undoped structure. Activation energies are reported in the text.

The ratio between the tracer and charge diffusion coefficients is named Haven ratio and provides information about the motion of carriers in the system [45, 48–50]. A Haven ratio, H , of 1 corresponds to uncorrelated Brownian motion, whereas lower values are an indication of coherent collective movements. Furthermore, a constant temperature Haven ratio implies an equality between the activation energies related to tracer diffusion and ionic conductivity. In LLZWO, we observe a similar behavior to that of the thio-lisicon electrolyte $\text{Li}_{10}\text{GeP}_2\text{S}_{12}$ [45], displaying comparable activation energies. In the case of undoped systems, we obtain $H \sim 0.3$, a value compatible with other recent simulation results [43, 50]. The same value is obtained for the Haven ratio of the implicitly and explicitly doped system. As discussed in Ref. [50] using nudged elastic bands (NEB) calculations, there is an understanding that diffusion events involving the simultaneous movement of different particles are much more favorable than single ion jumps. A similar conclusion can be reached considering the low value of the Haven ratio, which proves that the most probable, and therefore energetically favored, diffusion events involve a coherent particle motion. Our result suggests

that the same mechanism applies in the case of doped systems and therefore we can conclude that the local defects introduced by the dopant are not strong enough to decorrelate particle motion. Only in the unphysical case of the implicit doping model can we find a slight decrease of H and a small temperature dependence of the Haven ratio, which do not change the overall interpretative picture.

Site occupancy auto-correlation function

Finally, in order to shed further light on the mechanism and dynamics of the Li diffusion in doped and undoped LLZO structures, we also investigate the correlation of the occupancy of the Li sites described in Fig. 1. To this end, we map the set of binary variables $\sigma_I(\tau)$ associated with the occupation of a given site I at time τ (-1 when unoccupied and 1 when occupied) to the spin variables of an Ising model (down and up). The autocorrelation function is then averaged over the different realizations of the dopant distribution, as done in spin glass theory. For a single realization, we define the autocorrelation function as

$$C_\sigma(t) = \left\langle \langle \sigma_I(t_0) \sigma_I(t_0 + t) \rangle_{t_0} - \langle \sigma_I(t_0) \rangle_{t_0}^2 \right\rangle_I \quad (7)$$

where $\sigma_I(\tau)$ is, as previously defined, the instantaneous occupancy of the site I with value in $\{-1, 1\}$ and $\langle \sigma_I(t_0) \rangle_{t_0}$ corresponds to the time averaged occupancy of the site I and defines the initial departure from 1 at $t = 0$.

The calculation of the site occupancies was done using the following algorithm. We first define the tetrahedral sites as the center of mass of the four oxygen atoms coordinating the sites. Each Li-ion is then assigned to either a single or a pair of tetrahedral sites using a distance cutoff of 3.1 \AA . The ions assigned to pairs correspond to the ones occupying an octahedral site located between the two considered tetrahedral sites [51].

At $t = 0$, the auto-correlation function is equal to

$$C_\sigma(0) = \left\langle 1 - \langle \sigma_I(t_0) \rangle_{t_0}^2 \right\rangle_I \quad (8)$$

It is to be noted that this site occupancy does not correspond to the one reported in crystallographic measurements since (i) the occupancy of an empty site is set to -1 rather than to 0 and (ii) the number of crystallographic sites does not match the one resulting from

our assignment methods where octahedral sites are degenerate. In Fig. 9 we report the disorder-averaged autocorrelation curves $[C_\sigma(t)]_{\text{av}}$ computed for the undoped model, the implicit doping model with $x = 0.15$ and the explicit doping model with different doping fractions ($x = 0.15$ and 0.25) at three temperatures: 300, 400 and 500 K. The curves are presented averaged over all sites (global) and resolved into partial-averages over tetrahedral and octahedral sites.

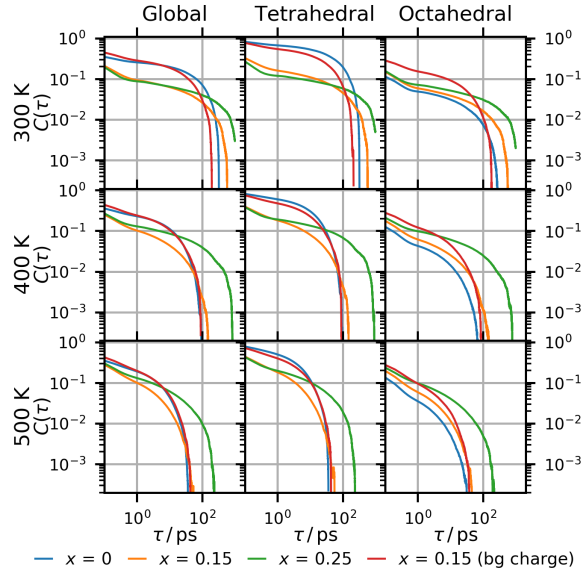


Figure 9. Global and site-type resolved autocorrelation functions of the site occupancy σ_i at 300 K, 400 K and 500 K for the undoped (**blue**), $x = 0.15$ (**orange**) and $x = 0.25$ (**green**) explicit doping, and $x = 0.15$ (**red**) implicit doping.

The autocorrelation functions show two distinct decay processes. The first one is extremely fast with a characteristic time of a few picoseconds and can be successfully fitted with a power law decay that takes the autocorrelation function to a plateau $c(t) = q_d$. The second process is much slower and fixes the time scale of the long time decay. This process shows a stronger temperature dependence and is best fitted with an exponential decay, typical of an ergodic diffusive behaviour [52]. The two regimes can be summarized as follows:

$$\begin{aligned}
 c(t) &\approx q_d + c_a t^{-a} & \text{for } c(t) > q_d, \\
 c(t) &\approx c_\beta e^{-\beta t} & \text{for } c(t) < q_d.
 \end{aligned}
 \tag{9}$$

The parameters of the fits for the first and second decays, a and β respectively, are given in Table II and show interesting trends as a function of the dopant concentration. The decay

Doping fraction	a			β / ps^{-1}		
	300 K	400 K	500 K	300 K	400 K	500 K
$x = 0$	1.015	0.673	0.514	0.011	0.058	0.139
$x = 0.15$	1.403	1.139	0.960	0.006	0.031	0.102
$x = 0.25$	1.882	1.469	1.157	0.002	0.004	0.017
$x = 0.15$	0.861	0.744	0.647	0.020	0.047	0.116

Table II. Fitting of the autocorrelation function of the site occupancies (Fig. 9) according to the model in Eq. 9. The first three lines report results for the explicit doping scheme, while the last one refers to the implicit doping model.

associated with the first process occurs on too fast a time-scale for it to be associated with the diffusive motion of the Li ions. We rather interpret it as the result of a fast non-diffusive scattering of the lithium ions around the different sites. In the explicit doping model, the increment of the dopant concentration correlates with an increase of the decay rate of the first process. This accelerated decay of the site occupancy correlation is consistent with increased scattering of the trapped lithium ions around the octahedral sites described in Fig. 5 and 6. This interpretation is further supported by the fact that the change in carrier concentration alone cannot account for the increased decay rate as the implicit model displays an opposite trend. The second, exponential decay of the autocorrelation function is instead related to the long scale diffusive process. Its dependence on doping concentration and doping scheme is coherent with the behavior observed for the diffusion coefficient and ionic conductivity as presented in Fig. 8. The implicit doping facilitates the long time diffusion by decreasing the cluttering through lowering of the concentration of charge carriers, leading to the faster decay of the autocorrelation function. Similarly to the first process, the trend is reversed in the explicit model where the correlation time is increased by the presence of the dopant hindering the diffusive process. These observations are coherent with the change similarly observed in the velocity autocorrelation function.

IV. CONCLUSION

In this work we investigated the thermodynamic and kinetic properties of doped LLZO by means of molecular dynamics simulations based on an ab-initio parametrized polarizable force-field.

Our results show that the overall quality of the force-field description is particularly good

at describing both the thermodynamic and kinetic aspects of the diffusion process in LLZO. We achieve this despite some discrepancies observed during the direct comparison of the activation energies of the doped systems with experimental data [24, 25]. While experiments point towards values around 0.45 eV, close to the activation energy of the undoped tetragonal phase, we observe values between 0.20 and 0.25 eV, closer to the high temperature experimental activation energy of the cubic phase. However, a word of caution is always needed when directly comparing simulations to experiments. In fact, while real materials are composed by nanostructures arranged in a disordered array, the simulations deal with perfectly periodic systems with no grain boundaries. In addition, the extraction of activation energies from experimental data also requires the use of models and therefore it cannot be unequivocally compared to the outcome of our simulations. What we aim at with this study is a qualitative understanding of the different trends associated with the increase of the dopants concentration, W ions, isolating the different contributions by means of specific analysis tools and theoretical ‘experiments’, e.g. the use of explicit versus implicit doping models. Despite the above mentioned discrepancies, the overall experimental trends are confirmed by our simulations.

We first observed that the distribution of the W dopant atoms affects the efficiency of the charge transport process. For this reason, in addition to the canonical ensemble average, we consider critical the use of an average over different realizations of the dopants distribution using an approach derived from spin glass theory. Overall, our results lead to the identification of two main effects induced by the introduction of the dopant, significantly affecting the conductivity of LLZO. The first is of a thermodynamic nature and relates to the stabilization of the conducting cubic phase at lower temperatures, which can clearly be identified as an effect of the lowering of the concentration of the charge carriers exclusively. The second, kinetic, is affected by both the change in the concentration of the carrier and the local modification of the potential energy landscape felt by the Li ions. The first contribution is isolated through the use of the implicit model, smearing the additional positive charge of the dopant uniformly over the entire simulation box. The analysis of the conductivity reveals a substantial decrease of the activation energy compared to the reference one, namely the undoped structure. This shows that the decrease of the Li concentration induced by doping results in the decongestion of the network of channels allowing a higher mobility of the Li. In addition, when considering the nature of the defects induced by the hypervalent dopants

(W centers in the explicit model), the additional coulombic repulsion promotes further scattering of the Li ions, causing an overall decrease of the conductivity and an increase of the activation energy, similar to the proton trapping effect in hydrogen conductors [53, 54]. This is also evident from the analysis of the Li ions distribution around the dopants, which shows a depletion after the first coordination shell associated with the breaking of the Li "wire" (Fig. 5 and 6). Interestingly, the analysis of the autocorrelation functions of the site occupancies (Fig. 9) confirms that the long term diffusive process slows down considerably as a result of the scattering W centers whereas the short time oscillation between neighboring sites is in general accelerated by the presence of the dopant.

In conclusion, our atomistic simulations reveal a very complex behavior of the LLZO conductivity as a function of the dopant concentration. While a quantitative description of the diffusion process is probably still beyond the capabilities of our simulations, our approach is able to capture the different trends due to both temperature and dopant concentration. This offers valuable insights into the interplay between thermodynamic phase stabilization and kinetic slow down mechanisms happening in the doped systems.

V. ACKNOWLEDGMENT

This research was supported by the NCCR MARVEL, funded by the Swiss National Science Foundation. This work was supported by a grant from the Swiss National Supercomputing Centre (CSCS) under project mr18.

-
- [1] D. H. P. Kang, M. Chen, and O. A. Ogunseitan, *Environ. Sci. Technol.* **47**, 5495 (2013).
 - [2] J. Christensen, P. Albertus, R. S. Sanchez-Carrera, T. Lohmann, B. Kozinsky, R. Liedtke, J. Ahmed, and A. Kojic, *J. Electrochem. Soc.* **159**, R1 (2012).
 - [3] F. MIZUNO, S. NAKANISHI, Y. KOTANI, S. YOKOISHI, and H. IBA, *Electrochemistry* **78**, 403 (2010).
 - [4] W. Xu, V. V. Viswanathan, D. Wang, S. A. Towne, J. Xiao, Z. Nie, D. Hu, and J.-G. Zhang, *J. Power Sources* **196**, 3894 (2011).
 - [5] S. A. Freunberger, Y. Chen, Z. Peng, J. M. Griffin, L. J. Hardwick, F. Bardé, P. Novák, and P. G. Bruce, *J. Am. Chem. Soc.* **133**, 8040 (2011).

- [6] T. Laino and A. Curioni, *Chemistry* **18**, 3510 (2012).
- [7] T. Laino and A. Curioni, *New J. Phys.* **15**, 095009 (2013).
- [8] S. Jeong, Y. Lim, Y. Choi, G. Cho, K. Kim, H. Ahn, and K. Cho, *J. Power Sources* **174**, 745 (2007).
- [9] S. Stramare, V. Thangadurai, and W. Weppner, *Chem. Mater.* **15**, 3974 (2003).
- [10] P. Knauth, *Solid State Ionics* **180**, 911 (2009).
- [11] A. Robertson, A. West, and A. Ritchie, *Solid State Ionics* **104**, 1 (1997).
- [12] G.-y. Adachi, N. Imanaka, and H. Aono, *Adv. Mater.* **8**, 127 (1996).
- [13] V. Thangadurai and W. Weppner, *Ionics (Kiel)*. **12**, 81 (2006).
- [14] V. Thangadurai, H. Kaack, and W. J. F. Weppner, *J. Am. Ceram. Soc.* **86**, 437 (2003).
- [15] S. Ohta, T. Kobayashi, and T. Asaoka, *J. Power Sources* **196**, 3342 (2011).
- [16] C. Deviannapoorani, L. Dhivya, S. Ramakumar, and R. Murugan, *J. Power Sources* **240**, 18 (2013).
- [17] S. Ramakumar, C. Deviannapoorani, L. Dhivya, L. S. Shankar, and R. Murugan, *Prog. Mater. Sci.* **88**, 325 (2017).
- [18] D. Rettenwander, P. Blaha, R. Laskowski, K. Schwarz, P. Bottke, M. Wilkening, C. A. Geiger, and G. Amthauer, *Chem. Mater.* **26**, 2617 (2014).
- [19] Y. Chen, E. Rangasamy, C. Liang, and K. An, *Chem. Mater.* **27**, 5491 (2015).
- [20] R. Jalem, M. J. D. Rushton, W. Manalastas, M. Nakayama, T. Kasuga, J. A. Kilner, and R. W. Grimes, *Chem. Mater.* **27**, 2821 (2015).
- [21] E. Rangasamy, J. Wolfenstine, J. Allen, and J. Sakamoto, *J. Power Sources* **230**, 261 (2013).
- [22] S. Mukhopadhyay, T. Thompson, J. Sakamoto, A. Huq, J. Wolfenstine, J. L. Allen, N. Bernstein, D. A. Stewart, and M. D. Johannes, *Chem. Mater.* **27**, 3658 (2015).
- [23] F. Chen, J. Li, Z. Huang, Y. Yang, Q. Shen, and L. Zhang, *J. Phys. Chem. C* **122**, 1963 (2018).
- [24] L. Dhivya, N. Janani, B. Palanivel, and R. Murugan, *AIP Adv.* **3** (2013), 10.1063/1.4818971.
- [25] Y. Li, Z. Wang, Y. Cao, F. Du, C. Chen, Z. Cui, and X. Guo, *Electrochim. Acta* **180** (2015), 10.1016/j.electacta.2015.08.046.
- [26] L. J. Miara, S. P. Ong, Y. Mo, W. D. Richards, Y. Park, J.-M. Lee, H. S. Lee, and G. Ceder, *Chem. Mater.* **25**, 3048 (2013).
- [27] Z. Cao, X. Cao, X. Liu, W. He, Y. Gao, J. Liu, and J. Zeng, *Ceram. Int.* **41**, 6232 (2015).

- [28] D. Rettenwander, G. Redhammer, F. Preishuber-Pflügl, L. Cheng, L. Miara, R. Wagner, A. Welzl, E. Suard, M. M. Doeff, M. Wilkening, J. Fleig, and G. Amthauer, *Chem. Mater.* **28**, 2384 (2016).
- [29] D. O. Shin, K. Oh, K. M. Kim, K.-Y. Park, B. Lee, Y.-G. Lee, and K. Kang, *Sci. Rep.* **5**, 18053 (2016).
- [30] S. Adams and R. P. Rao, *J. Mater. Chem.* **22**, 1426 (2012).
- [31] M. Klenk and W. Lai, *Phys. Chem. Chem. Phys.* **17**, 8758 (2015).
- [32] B. G. Dick and A. W. Overhauser, *Phys. Rev.* **112**, 90 (1958).
- [33] S. Plimpton, *J. Comput. Phys.* **117**, 1 (1995).
- [34] D. Marx and J. Hutter, “Ab-initio Molecular Dynamics: Theory and Implementation,” in *Mod. Methods Algorithms Quantum Chem.*, NIC, edited by J. Grotendorst (Forschungszentrum Jülich, 2000) Chap. 13, pp. 301–449, i ed.
- [35] W. Andreoni and A. Curioni, *Parallel Comput.* **26**, 819 (2000).
- [36] S. Goedecker, M. Teter, and J. Hutter, *Phys. Rev. B* **54**, 1703 (1996).
- [37] M. Ceriotti, G. Bussi, and M. Parrinello, *Phys. Rev. Lett.* **102**, 020601 (2009).
- [38] M. Ceriotti, G. Bussi, and M. Parrinello, *J. Chem. Theory Comput.* **6**, 1170 (2010), arXiv:arXiv:1204.0822v1.
- [39] R. E. Jones and K. K. Mandadapu, *J. Chem. Phys.* **136**, 154102 (2012).
- [40] S. F. Edwards and P. W. Anderson, *J. Phys. F Met. Phys.* **5**, 965 (1975).
- [41] B. Sadigh, P. Erhart, A. Stukowski, A. Caro, E. Martinez, and L. Zepeda-Ruiz, *Phys. Rev. B - Condens. Matter Mater. Phys.* **85**, 184203 (2012), arXiv:1012.5082.
- [42] G. Larraz, A. Orera, M. L. Sanjuán, H. Hayakawa, K. I. Ohshima, J. Akimoto, M. L. Saboungi, N. Kim, T. Pettke, W. Weppner, V. Duppel, L. Kienle, and J. Janek, *J. Mater. Chem. A* **1**, 11419 (2013).
- [43] M. J. Klenk and W. Lai, *Solid State Ionics* **289** (2016), 10.1016/j.ssi.2016.03.002.
- [44] M. I. Barker and T. Gaskell, *J. Phys. C Solid State Phys.* **5**, 353 (1972).
- [45] A. Marcolongo and N. Marzari, *Phys. Rev. Mater.* **1**, 025402 (2017).
- [46] M. Matsui, K. Takahashi, K. Sakamoto, A. Hirano, Y. Takeda, O. Yamamoto, and N. Imanishi, *Dalt. Trans.* **43**, 1019 (2014).
- [47] J. Allen, J. Wolfenstine, E. Rangasamy, and J. Sakamoto, *J. Power Sources* **206**, 315 (2012).
- [48] G. E. Murch, *Philos. Mag. A* **45**, 685 (1982).

- [49] B. J. Morgan and P. A. Madden, *Phys. Rev. Lett.* **112**, 145901 (2014).
- [50] X. He, Y. Zhu, and Y. Mo, *Nat. Commun.* **8**, 15893 (2017).
- [51] This method is not able to resolve the two individual octahedral sites. However, because of the close proximity of the two sites, the probability of them both being occupied is extremely low. This shortcoming is therefore not an issue.
- [52] F. Caltagirone, G. Parisi, and T. Rizzo, *Phys. Rev. E - Stat. Nonlinear, Soft Matter Phys.* **85**, 051504 (2012), arXiv:arXiv:1202.5751v2.
- [53] Y. Yamazaki, F. Blanc, Y. Okuyama, L. Buannic, J. C. Lucio-Vega, C. P. Grey, and S. M. Haile, *Nat. Mater.* **12**, 647 (2013).
- [54] A. Fluri, A. Marcolongo, V. Roddatis, A. Wokaun, D. Pergolesi, N. Marzari, and T. Lippert, “Enhanced Proton Conductivity in Y-Doped BaZrO₃ via Strain Engineering,” (2017).
- [55] M. P. Allen and D. J. Tildesley, *Computer Simulation of Liquids*, Vol. 1 (Oxford University Press, 2017).
- [56] D. Frenkel and B. Smit, *Understanding Molecular Simulation* (Elsevier, 2002) p. 638.
- [57] J.-P. Boon and S. Yip, *Molecular hydrodynamics* (Dover Publications, 1991) p. 417.
- [58] R. Chitra and S. Yashonath, *J. Phys. Chem. B* **101**, 5437 (1997).
- [59] X. He, Y. Zhu, A. Epstein, and Y. Mo, *npj Comput. Mater.* **4**, 18 (2018).
- [60] L. Ercole, A. Marcolongo, and S. Baroni, *Sci. Rep.* **7**, 15835 (2017).

Appendix A: Force-fitting

The fitting of the force-field was achieved using forces and energies calculated at DFT level using the plane-wave CPMD software package [34, 35]. The PBE functional and norm-conserving Goedecker pseudopotentials [36] were used in conjunction with a cutoff of 150 Ry. Fig. 10 and 11 shows comparison between the reference DFT equation of states and forces and the ones of the force-field respectively.

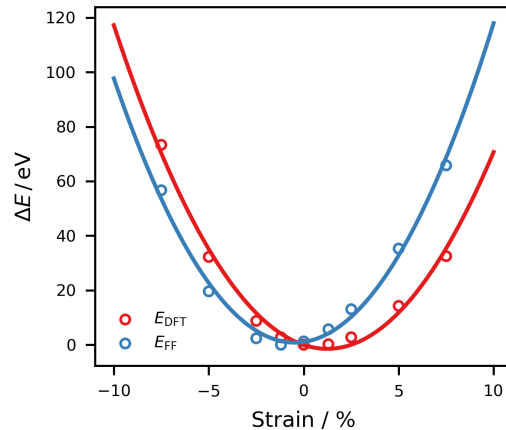


Figure 10. Reference DFT and force-field energies as a function off applied strain.

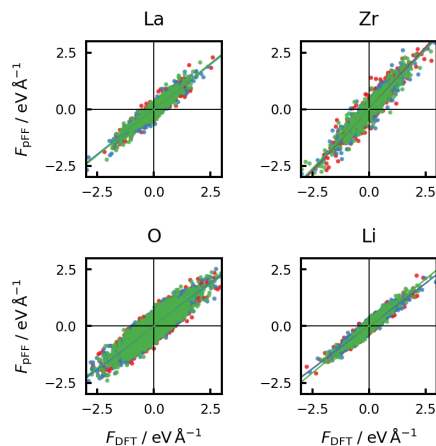


Figure 11. DFT and force-field forces on Li, La, Zr and O evaluated for the initial training used for the parametrization of the force-field.

Appendix B: GLE versus NVE simulations

NVE simulations have been a preferred method for the determination of the ionic conductivity in previous works [20, 31]. Although this method may be optimal for classical force-fields, the use of a core-shell model changes the situation. The temperature of the shells should be kept as low as possible to keep a shell distribution as sharp as possible around their equilibrium positions. The control of the temperature of the shell is therefore an important aspect of simulations implementing a core-shell model. Despite the possibility to apply thermostats to the center of mass of the core-shells pairs during the equilibration process, yielding lower shell temperatures, they usually remain comparable to the ionic one. Furthermore, bleeding of energy can be observed from the cores to the shells as illustrated in Fig. 12. Although the constant use of a thermostat can have an impact on the dynamic and

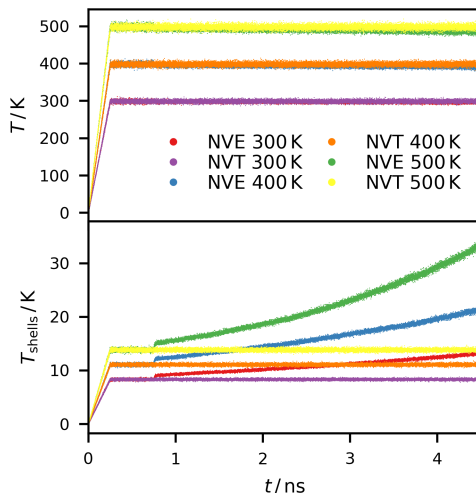


Figure 12. Plot of the system (**Top**) and shell (**Bottom**) temperatures during NVE and NVT simulations at target temperatures 300 K, 400 K and 500 K. Energy bleeding from the cores to the shells can be observed in the case of the NVE simulations.

the correlation times in the system, Fig. 13 shows that it has little impact on the activation energy of the system with variation in the activation energy inferior to 10%.

Appendix C: Diffusion coefficients and long tails

In this appendix we summarize the formal identities needed to link the long time decay of the derivative of the mean squared displacement and the velocity autocorrelation function.

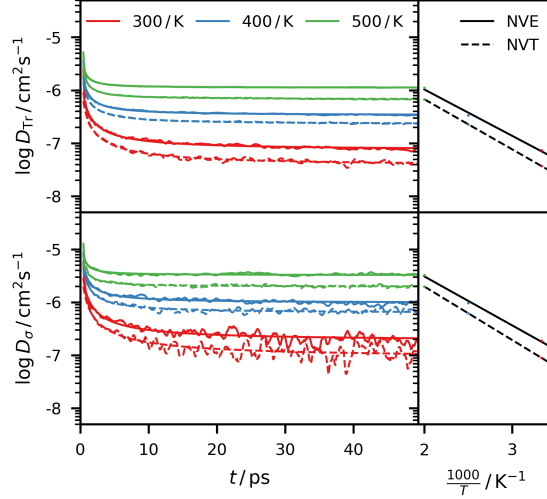


Figure 13. **Left** Comparison between the NVE and NVT convergence of the charge and tracer diffusion coefficient of the Li ion with the time lag (see eq. (C9)) for the $x = 0.15$ doped system. **Right** The Arrhenius plots correspond to the t^{-1} fit of the diffusion coefficient.

The tracer and charge diffusion coefficients [55–57] can be written in terms of the respective autocorrelation functions :

$$D_{\text{Tr}} = \frac{1}{3} \int_0^{+\infty} C_v(t') dt', \quad (\text{C1})$$

$$D_{\sigma} = \frac{N_{\text{Li}}}{3} \int_0^{+\infty} C_V(t') dt', \quad (\text{C2})$$

where:

$$C_v(t) = \langle \mathbf{v}_i(t_0 + t) \mathbf{v}_i(t_0) \rangle_{i,t_0}, \quad (\text{C3})$$

$$C_V(t) = \langle \langle \mathbf{v}_i(t_0 + t) \rangle_i \langle \mathbf{v}_i(t_0) \rangle_i \rangle_{t_0}. \quad (\text{C4})$$

$\mathbf{v}_i(t)$ is the velocity of lithium i at time (t), N_{Li} the number of lithium atoms, $C_v(t)$ the single particle velocity autocorrelation and $C_V(t)$ the velocity autocorrelation function of the lithium centre of mass. As explained in Ref. [45], all quantities must be computed in the frame of reference of the rigid matrix in order to correct for nonphysical drifts.

We focus on tracer diffusion, even if all arguments apply to charge diffusion as well. Equation C1 is called the Einstein identity and derived as the long time limit of the following relation between the mean squared displacement and the velocity autocorrelation function

[56] :

$$\left\langle |\mathbf{x}_i(t_0 + t) - \mathbf{x}_i(t_0)|^2 \right\rangle_{i,t_0} = 2t \int_0^t C_v(t') \left(1 - \frac{t'}{t}\right) dt' \quad (\text{C5})$$

Instead of directly performing the infinite limit, one can differentiate twice this identity with respect to t :

$$\frac{\partial \left\langle |\mathbf{x}_i(t_0 + t) - \mathbf{x}_i(t_0)|^2 \right\rangle_{i,t_0}}{\partial t} = 2 \int_0^t C_v(t') dt' \quad (\text{C6})$$

$$\frac{\partial^2 \left\langle |\mathbf{x}_i(t_0 + t) - \mathbf{x}_i(t_0)|^2 \right\rangle_{i,t_0}}{\partial t^2} = 2C_v(t) \quad (\text{C7})$$

Note that these identities are valid for any t . Equation (C6) and (C2) provide a formal proof of the intuitive relation:

$$D_{\text{Tr}} = \lim_{t \rightarrow \infty} D_{\text{Tr}}(t) \quad (\text{C8})$$

$$D_{\text{Tr}}(t) = \frac{1}{6} \frac{\partial \left\langle |\mathbf{x}_i(t_0 + t) - \mathbf{x}_i(t_0)|^2 \right\rangle_{i,t_0}}{\partial t}, \quad (\text{C9})$$

also exploited in this work in Equation (6), where a time dependent diffusion coefficient $D_{\text{Tr}}(t)$ has been defined as the derivative of mean squared displacement at a time lag t . Equation (C7) instead shows that the second order derivative of the mean squared displacement is exactly equal to the velocity autocorrelation function. We therefore deduce that the polynomial decay of the velocity autocorrelation measured in our simulations of Garnet materials as $C_v(t) \sim A_2 t^{-a}$, $a > 1$, leads to a slow convergence to the transport coefficient in equation (C9), since it forces the long time dependence $\frac{\partial \left\langle |\mathbf{x}_i(t_0 + t) - \mathbf{x}_i(t_0)|^2 \right\rangle}{\partial t} \sim D_{\text{Tr}} + A_1 t^{-(a-1)}$. This last relation has therefore been used for long time extrapolations.

Finally, in Fig. 14, as an example, we report a log-log plot of the tail of the single-particle velocity autocorrelation function, in an explicitly doped system and at a temperature of 300K , showing the t^{-2} asymptotic behavior cited in the text. An alternative confirmation of this result follows by plotting the functions $C_v(t)t^k$ and checking for which values of k a convergence to a finite limit, different from zero, is observed before the signal-to-noise ratio becomes too large. This approach is exemplified in Fig. 15.

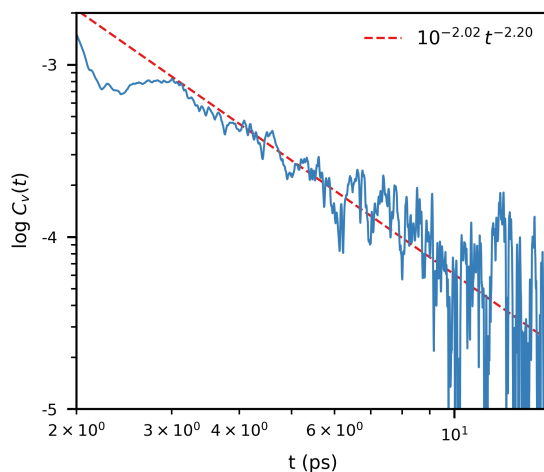


Figure 14. Log-log plot of the tail of the single-particle velocity autocorrelation function for the explicitly doped system at $300K$, after filtering with a window of 2.4ps in order to remove high frequency noise.

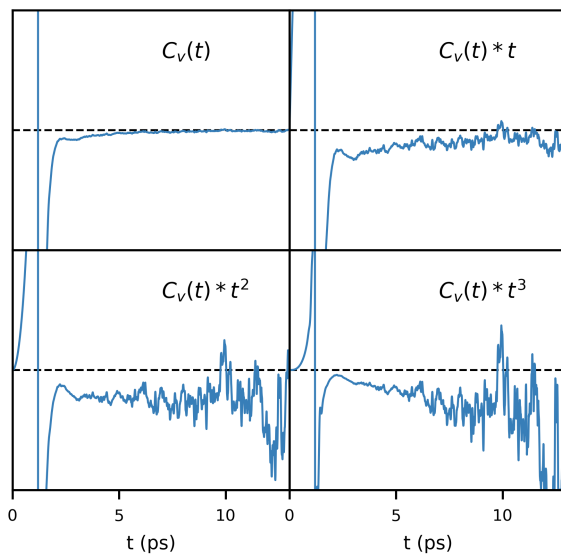


Figure 15. Alternative check of the t^{-2} decay of the velocity autocorrelation function for the explicitly doped system. In this case $C_v(t)t^k$ tends to zero for $k = 0, 1$, to a finite limit for $k = 2$, and diverges linearly for $k = 3$. The same filtering was applied as in Fig. 14

Appendix D: Sampling uncertainty versus configurational noise

When considering explicitly doped systems, two kinds of uncertainty affect the estimation of $D(t_{lag})$, defined in appendix C, eq. (C9), as the derivative of the mean squared displacement at time lag t_{lag} . The first contribution arises from the dependence of the

diffusion coefficient from the dopant configuration and can be denoted as *configurational noise*. This contribution goes to zero in the limit of infinitely large simulation cells. The second contribution originates from the finite simulation time length T at a fixed dopant configuration and we call it *sampling noise*. In the following we derive metrics to evaluate the two types of noise in the simulation of doped materials at a fixed simulation cell size.

First we discuss sampling noise and we denote the standard deviation due to the finite sampling as $\sigma_{t_{lag}, \Gamma_D}^{\text{SAMP}}(T)$, dependent both on the explicit dopant configuration Γ_D and on the finite simulation time T . From now on in the expressions for the standard deviations we insert t_{lag} as a suffix and consider it as a parameter. Sampling noise can be numerically estimated for a fixed configuration via block-analysis techniques, i.e. by dividing the trajectory into blocks and calculating the standard error of the mean [39]. This error is expected to decay as $\frac{1}{\sqrt{T}}$, where T is the simulation time. In particular, it tends to zero for large T , when the simulation is long enough to determine exactly the value of the diffusion coefficient at a fixed configuration Γ_D . Sampling noise is the only one which must be considered in simulations of undoped materials [39, 58, 59], or in an implicit doping setting. In the case of an explicitly doped material under analysis, an additional mean over configurations, as explained in the main text, can be performed:

$$\sigma_{t_{lag}}^{\text{SAMP}}(T) \equiv \left[\sigma_{t_{lag}, \Gamma_D}^{\text{SAMP}}(T) \right]_{av}. \quad (\text{D1})$$

This function can be then be plotted as a function of T , for a fixed time lag t_{lag} . $\sigma_{t_{lag}}^{\text{SAMP}}(T)$ quantifies the mean effect of sampling noise alone. It does not reflect configurational noise since each term $\sigma_{t_{lag}, \Gamma_D}^{\text{SAMP}}(T)$ considers only fluctuations over the configuration dependent equilibrium value.

We now move to configurational noise and indicate explicitly with $D_{\Gamma_D}(t_{lag})$ the exact value of the diffusion coefficient at a fixed dopant configuration. Looking at the spread among configurations we define:

$$\sigma_{t_{lag}}^{\text{DOP}} \equiv \left[(D_{\Gamma_D}(t_{lag}) - [D_{\Gamma_D}(t_{lag})]_{av})^2 \right]_{av}^{1/2} \quad (\text{D2})$$

Of course one does not know the exact value of $D_{\Gamma_D}(t_{\text{lag}})$, but by replacing $D_{\Gamma_D}(t_{\text{lag}})$ with its standard estimator at a simulation time T we get a stochastic variable $\hat{\sigma}_{t_{\text{lag}}}^{\text{DOP}}(T) \rightarrow \sigma_{t_{\text{lag}}}^{\text{DOP}}$ for $T \rightarrow \infty$ which can be used as an estimator for long times T (we use here the standard notation of indicating stochastic variables with a hat [60]). Practically, when plotting $\hat{\sigma}_{t_{\text{lag}}}^{\text{DOP}}(T)$ as a function of T , a plateau has to be reached. This plateau, $\sigma_{t_{\text{lag}}}^{\text{DOP}}$, is dependent on configurational noise alone and can be considered as a measure of the configurational degrees of freedom due to the finite volume of the simulation cells used.

One can get a feeling of the magnitude of the two contributions comparing on the same plot, as done in Fig. 16 for the Tungsten-doped LLZO, $\hat{\sigma}_{t_{\text{lag}}}^{\text{DOP}}(T)$ and $\sigma_{t_{\text{lag}}}^{\text{SAMP}}(T)$ as a function of T . We stress nevertheless again that only the asymptotic value for large T of $\hat{\sigma}_{t_{\text{lag}}}^{\text{DOP}}(T)$ has a well defined deterministic meaning, whereas $\sigma_{t_{\text{lag}}}^{\text{SAMP}}(T)$, the variance at a finite time T , is a well defined deterministic quantity for every T . In order to estimate means over dopant configurations, as in Fig. 7 of the main text, technically the diffusion coefficients are needed to be known with infinite precision for every dopant distribution. Nevertheless, the previous analysis and Fig. 16 show that the simulation time T reaches the regime where $\sigma_{t_{\text{lag}}}^{\text{SAMP}}(T) \ll \sigma_{t_{\text{lag}}}^{\text{DOP}}$. Under this condition one is able to estimate configurational spreads and clearly distinguish between configurational and sampling noise, making it possible to characterize separately the contribution of configurational noise, as in Fig. 7 of the main text.

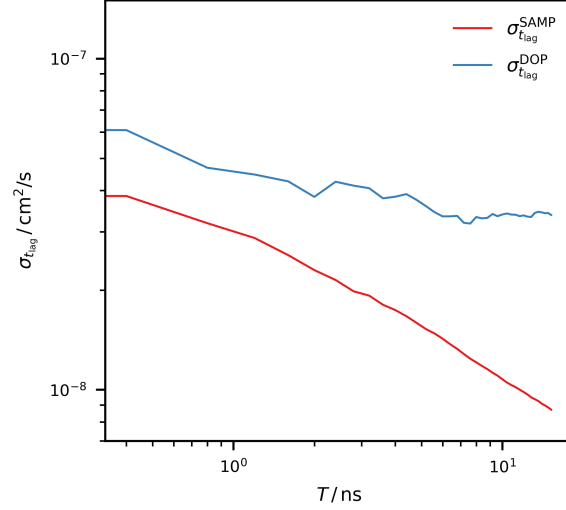


Figure 16. We show, as a function of simulation time T , the log-log plot of $\sigma_{t_{\text{lag}}}^{\text{SAMP}}(T)$ and the estimator $\hat{\sigma}_{t_{\text{lag}}}^{\text{DOP}}(T) \rightarrow \sigma_{t_{\text{lag}}}^{\text{DOP}}$ for $t_{\text{lag}} = 22.5$ ps and the charge diffusion coefficient. 4 initial lithium distributions for every dopant configuration are considered in order to increase the length of the trajectory. We see a linear decay of the sampling noise, compatible with the $T^{-1/2}$ behavior expected theoretically, whereas the estimator of configurational noise remains stable to a much higher value, showing that simulations time T are large enough so that the limit $\sigma_{t_{\text{lag}}}^{\text{SAMP}}(T) \ll \sigma_{t_{\text{lag}}}^{\text{DOP}}$ is satisfied.